

Numerical Verification of Full Waveform Inversion for the Chang'E-5 Lunar Penetrating Array Radar

Jing Li¹, Hai Liu², and Lige Bai¹

¹Jilin University

²guangzhou university

November 24, 2022

Abstract

One of the scientific payloads of Chang'E-5 (CE-5), i.e., the lunar penetrating array radar (LRPR), will carry out the in situ exploration of the regolith structure and guide the drilling sampling process. To evaluate the performance of the LRPR system, we present a multifrequency full-waveform inversion (FWI) with the total variation (TV) regularization constraint using simulated CE-5 LRPR data for imaging the regolith structure and estimating the physical parameters (permittivity and conductivity). The multifrequency FWI strategy is used to improve the inversion resolution, which updates the low-frequency gradient for the deep region and then increases the frequency range to update the shallow region. The TV regularization constraint not only reduces the gradient noise but also improves the inversion accuracy of local structures. To evaluate the actual LRPR measurement scenario, we use the actual source wavelet obtained from the LRPR instrument prototype in a ground lab to replace the theoretical Ricker wavelet. The actual source includes the effect of antenna radiation patterns and clutter noise from the metallic lander. Two typical heterogeneous lunar regolith model tests demonstrate that the proposed FWI scheme effectively reduces the lander metal impact, provides a reliable way to estimate the lunar regolith physical parameters and image the subsurface structures.

Numerical Verification of Full Waveform Inversion for the Chang'E-5 Lunar Penetrating Array Radar

Jing Li, *Member IEEE*, Hai Liu, *Senior Member IEEE* and Lige Bai

Abstract—One of the scientific payloads of Chang'E-5 (CE-5), i.e., the lunar penetrating array radar (LRPR), will carry out the in situ exploration of the regolith structure and guide the drilling sampling process. To evaluate the performance of the LRPR system, we present a multifrequency full-waveform inversion (FWI) with the total variation (TV) regularization constraint using simulated CE-5 LRPR data for imaging the regolith structure and estimating the physical parameters (permittivity and conductivity). The multifrequency FWI strategy is used to improve the inversion resolution, which updates the low-frequency gradient for the deep region and then increases the frequency range to update the shallow region. The TV regularization constraint not only reduces the gradient noise but also improves the inversion accuracy of local structures. To evaluate the actual LRPR measurement scenario, we use the actual source wavelet obtained from the LRPR instrument prototype in a ground lab to replace the theoretical Ricker wavelet. The actual source includes the effect of antenna radiation patterns and clutter noise from the metallic lander. Two typical heterogeneous lunar regolith model tests demonstrate that the proposed FWI scheme effectively reduces the lander metal impact, provides a reliable way to estimate the lunar regolith physical parameters and image the subsurface structures.

I. INTRODUCTION

The Lunar Penetrating Radar (LPR) is a nondestructive, high-resolution, and high-efficiency tool that has been used for on-ground exploration of the subsurface structure of the Moon [1]. A standard LPR system carried by Chang'E-3 (CE-3) recorded a radar image to reveal the significant stratigraphic zones of the northern Mare Imbrium in 2013 [1]-[3]. A similar LPR system carried by CE-4 was launched at the end of 2018 and landed at the south pole Aitken (SPA) basin on the far side of the Moon [4]. At the end of 2020, as the third phase of the Chinese Lunar Exploration Program (CLEP), CE-5 will plan to launch, and lunar regolith penetrating array radar (LRPR) will be equipped at the bottom of the lander to detect the subsurface regolith structure. The drilling equipment will drill a sample of the lunar regolith structure of the landing site for the sample return mission [5]. Compared with previous common-offset LPR, multi-offset LRPR has the Vivaldi antenna array fixed on the bottom of the lander, which includes 12 antennas working in a single-input and multi-output (SIMO) work mode. The antenna center frequency is approximately 2 GHz. One antenna transmits the radar waves, and all of the other

11 antennas receive the reflection signal. After each antenna has completed the transmission, the LRPR achieves the in situ exploration for the drilling area [5]. This is the first time that such an array radar (multi-offset) has been applied in Moon structure exploration [6].

In the usual common-offset LPR, the information about each subsurface point comes from a single ray. The multioffset LRPR records data from multiple rays and obtains enhanced lunar regolith images and high-resolution information about physical properties. The tomographic inversions of multi-offset radar data are generally based on geometrical ray theory or full-waveform inversion (FWI). The resolution provided by ray-based tomography is limited by the ray information causing insufficient resolution that is approximately the diameter of the first Fresnel zone [7],[8]. For a high-resolution image, the FWI method has been widely applied in seismic data (acoustic or elastic waves) [9],[10] and ground-penetrating radar data (GPR, electromagnetic wave)[11],[12],[13].

FWI is a promising technique to quantitatively image subsurface structures, which takes full use of waveform information and results in a high lateral resolution on the order of half wavelengths [10]. However, almost all successful FWIs rely on accurate initial models, where most misfit functionals of FWI can be easily trapped into local minima due to the famous cycle-skipping issue. Remedies to this problem tend to utilize the information hidden in the low-frequency signals of the recorded radar data. One of the most successful methods is the multiscale approach[14], which gradually inverts for permittivity or conductivity models with low-to-higher wavenumbers [13]. In addition, we need to simultaneously invert both the permittivity and conductivity parameters. The problem of inverting multiple physical parameters using FWI is complicated by interparameter trade-offs arising from inherent ambiguities between different physical parameters. Regularization techniques are required to decrease the sensitivity of FWI to the initial model and noise and reduce the ill-posedness of the problem resulting from uneven illumination [15],[16].

In this paper, we present the time-domain multifrequency FWI with a total variation (TV) constraint to evaluate the performance of LRPR data on the estimation of physical parameters (permittivity and conductivity) and the imaging of the regolith structure by lunar regolith numerical model tests. We build the same model size and measurement parameter according to the LRPR system ground experiment. The actual source wavelet, which is measured by the LRPR instrument prototype as measured in the ground experiment, is the input source in the FWI test. It includes the effect of the antenna radiation patterns and clutter noise from the metallic lander.

This work is supported by the Natural Science Foundation of China (41874134, 41874120), the Jilin Excellent Youth Fund (20190103142JH), and the China Postdoctoral Science Foundation 2015M571366 (Corresponding author: Hai Liu e-mail:hliu@gzhu.edu.cn). J. Li and L. Bai are with the College of Geo-exploration Science and Technology, Jilin University, Changchun, Jilin. 130012, China. H. Liu is with the School of Civil Engineering, Guangzhou University, Guangzhou, 510006, China

This paper is organized into four parts. After the introduction, we explain the theory of multifrequency FWI and how it is used for LRPR data inversion. This includes the use of the implicit function theorem to derive the wave-equation formulas for the misfit gradient. Part three presents the numerical LRPR FWI tests for applying this method to the typical regolith model data set[17],[18]. The last section presents the conclusions.

II. SIMULTANEOUS TIME-DOMAIN FULL WAVEFORM INVERSION THEORY

The FWI method includes the following steps: 1) define a connective function that connects the data residual to the model parameters (permittivity ϵ and conductivity σ), 2) build a misfit function, which is the squared summation of the residuals between the predicted and the observed data, and 3) derive the gradient of the misfit function with respect to ϵ and σ in the time domain. We begin the theory from the 2D TM mode Maxwell equations[19],

$$\begin{aligned} -\mu \frac{\partial H_x}{\partial t} &= \frac{\partial E_z}{\partial y}, \\ \mu \frac{\partial H_y}{\partial t} &= \frac{\partial E_z}{\partial x}, \\ \epsilon \frac{\partial E_z}{\partial t} + \sigma E_z &= \frac{\partial H_y}{\partial x} - \frac{\partial H_x}{\partial y} + f(t), \end{aligned} \quad (1)$$

where ϵ , μ and σ are the permittivity, magnetic permeability, and conductivity parameters, respectively; E and H are the electric and magnetic field vectors; and $f(t)$ represents a point source function. We define a connective function that connects the waveform data residuals to the model physical parameters.

A. Connective Function

Let $\tilde{E}_d(\mathbf{x}_r, t; \mathbf{x}_s)$ denote a predicted event for a given initial permittivity model recorded at the receiver location \mathbf{x}_r , a source excited at time $t = 0$ and at location \mathbf{x}_s . d is the data that can be obtained from its waveform. Similarly, let $E_{d-\Delta d}(\mathbf{x}_r, t; \mathbf{x}_s)$ denote the same event in the observed data. Δd is the waveform difference between the predicted and observed data. The similarity between the observed and predicted data can be written as [20]

$$\begin{aligned} F_d(\mathbf{x}_r, t; \mathbf{x}_s) &= \int dt \frac{E_{d-\Delta d}(\mathbf{x}_r, t; \mathbf{x}_s)}{A_1(\mathbf{x}_r; \mathbf{x}_s)} \frac{\tilde{E}_d(\mathbf{x}_r, t; \mathbf{x}_s)}{A_2(\mathbf{x}_r; \mathbf{x}_s)} \\ &= \int dt \frac{E_{d-\Delta d}(\mathbf{x}_r, t; \mathbf{x}_s)}{A(\mathbf{x}_r; \mathbf{x}_s)} \tilde{E}_d(\mathbf{x}_r, t; \mathbf{x}_s), \end{aligned} \quad (2)$$

Here, $A_1(\mathbf{x}_r; \mathbf{x}_s)$ and $A_2(\mathbf{x}_r; \mathbf{x}_s)$ are the amplitude normalization factors for the observed and predicted data, respectively. We normalize the observed and predicted data so that their maximum amplitudes are equal to 1

$$A(\mathbf{x}_r; \mathbf{x}_s) = A_1(\mathbf{x}_r; \mathbf{x}_s) * A_2(\mathbf{x}_r; \mathbf{x}_s). \quad (3)$$

We seek to minimize the data residuals between the observed and predicted data. If the predicted and observed data have the same waveform, the normalized cross-correlation objective function in (2) will be maximized. The derivative of

$F_d(\mathbf{x}_r, t; \mathbf{x}_s)$ with respect to d should then be zero at $d = \Delta d$. Thus,

$$\begin{aligned} \dot{F}_{\Delta d} &= \left[\frac{\partial F_d(\mathbf{x}_r, t; \mathbf{x}_s)}{\partial d} \right]_{d=\Delta d} \\ &= \int dt \frac{\dot{E}_{d-\Delta d}(\mathbf{x}_r, t; \mathbf{x}_s)}{A(\mathbf{x}_r; \mathbf{x}_s)} \tilde{E}_d(\mathbf{x}_r, t; \mathbf{x}_s) = 0, \end{aligned} \quad (4)$$

where $\dot{E}_d(\mathbf{x}_r, t; \mathbf{x}_s) = \partial E_d(\mathbf{x}_r, t; \mathbf{x}_s) / \partial d$. (4) is the connective function, which will be used later to derive the Fréchet derivative of ϵ and σ .

B. Misfit Function

The FWI method attempts to determine the physical parameter (ϵ and σ) model that predicts LPR data that minimizes the misfit function[11]

$$\gamma = \frac{1}{2} \sum_s \sum_r \Delta d(\mathbf{x}_r, \mathbf{x}_s)^2, \quad (5)$$

where Δd is defined in the previous section and the summation in (5) is over all the sources and receivers. The gradients of the misfit function with respect to ϵ and σ are given by

$$\begin{aligned} \gamma_\epsilon(\mathbf{x}) &= -\frac{\partial \gamma}{\partial \epsilon} = -\sum_s \sum_r \left(\frac{1}{A^2} \frac{\partial \Delta d}{\partial \epsilon} \Delta d \right), \\ \gamma_\sigma(\mathbf{x}) &= -\frac{\partial \gamma}{\partial \sigma} = -\sum_s \sum_r \left(\frac{1}{A^2} \frac{\partial \Delta d}{\partial \sigma} \Delta d \right), \end{aligned} \quad (6)$$

From (4), we can obtain the following 3 equations for permittivity ϵ (the result for σ is similar):

i)

$$\begin{aligned} \dot{F}_{\Delta d}(\Delta d, \epsilon(\mathbf{x})) &= 0, \\ \Rightarrow \frac{\partial \dot{F}_{\Delta d}}{\partial \Delta d} \frac{\partial \Delta d}{\partial \epsilon(\mathbf{x})} + \frac{\partial \dot{F}_{\Delta d}}{\partial \epsilon(\mathbf{x})} &= 0, \\ \Rightarrow \frac{\partial \Delta d}{\partial \epsilon(\mathbf{x})} &= -\frac{\frac{\partial \dot{F}_{\Delta d}}{\partial \epsilon(\mathbf{x})}}{\frac{\partial \dot{F}_{\Delta d}}{\partial \Delta d}}, \end{aligned} \quad (7)$$

ii)

$$\frac{\partial \dot{F}_{\Delta d}}{\partial \Delta d} = \int dt \frac{\dot{E}_{d-\Delta d}(\mathbf{x}_r, t; \mathbf{x}_s)}{A(\mathbf{x}_r; \mathbf{x}_s)} \tilde{E}_d(\mathbf{x}_r, t; \mathbf{x}_s). \quad (8)$$

iii)

$$\frac{\partial \dot{F}_{\Delta d}}{\partial \epsilon(\mathbf{x})} = \int dt \frac{\dot{E}_{d-\Delta d}(\mathbf{x}_r, t; \mathbf{x}_s)}{A(\mathbf{x}_r; \mathbf{x}_s)} \frac{\partial \tilde{E}_d(\mathbf{x}_r, t; \mathbf{x}_s)}{\partial \epsilon(\mathbf{x})}. \quad (9)$$

Using (6)-(9), the gradient can be written as

$$\gamma_\epsilon(\mathbf{x}) = \sum_s \sum_r \frac{\partial \dot{F}_{\Delta d}}{\partial \epsilon(\mathbf{x})} \frac{\partial \Delta d}{\partial \Delta d} \Delta d(\mathbf{x}_r, \mathbf{x}_s). \quad (10)$$

The Fréchet derivative $\frac{\partial \tilde{E}_d(\mathbf{x}_r, t; \mathbf{x}_s)}{\partial \epsilon(\mathbf{x})}$ is derived in the next subsection.

C. Fréchet Derivative

To obtain the Fréchet derivative of the electric field (E) with respect to the perturbation $\epsilon(\mathbf{x})$ or $\sigma(\mathbf{x})$, a perturbation of $\epsilon \rightarrow \epsilon + \delta\epsilon$ or $\sigma \rightarrow \sigma + \delta\sigma$ will produce perturbed wavefields $\delta \tilde{E}_d$. The derivation of the gradient for the FWI inversion uses

the adjoint-state method. We can rewrite the gradient in (10) as

$$\begin{aligned}\gamma_\epsilon(\mathbf{x}) &= \sum_s \sum_r \frac{\partial \hat{F}_{\Delta d}}{\partial \epsilon(\mathbf{x})} \Delta d, \\ &= \sum_s \sum_r \frac{1}{K} \frac{\partial \hat{F}_{\Delta d}}{\partial \epsilon(\mathbf{x})} \Delta f, \\ &= -\frac{1}{K} \sum_s \int \left(\frac{\partial E_z}{\partial t} * \hat{E}_z \right) dt,\end{aligned}\quad (11)$$

The details of the adjoint-state method are shown in the Appendix. The gradient in (11) is computed by a zero-lag cross-correlation of a forward propagated source wavefield term and a backpropagated residuals wavefield term. The residual wavefield is calculated by weighting the observed data with their corresponding waveform residuals Δd . These weighted residuals can be used as an adjoint source from the receiver side.

D. Model Update

After computing the gradient, the conjugate gradient (CG) method is used to iteratively update the ϵ and σ models:

$$\begin{aligned}\sigma(\mathbf{x})^{(n+1)} &= \sigma(\mathbf{x})^{(n)} + \alpha_\sigma \frac{\partial \gamma}{\partial \sigma} + \alpha \gamma(\sigma)_{TV}, \\ \epsilon(\mathbf{x})^{(n+1)} &= \epsilon(\mathbf{x})^{(n)} + \alpha_\epsilon \frac{\partial \gamma}{\partial \epsilon} + \alpha \gamma(\epsilon)_{TV},\end{aligned}\quad (12)$$

where n denotes the index of the iteration, α_ϵ and α_σ are the step lengths, and α controls the contributions from the regularization term. γ_{TV} is the regularization term that uses the TV regularization to smooth the gradient.

E. Workflow for Multifrequency FWI with TV

The LRPR signal has a certain bandwidth. We use the Wiener filter method to decompose the LRPR signal into different frequency components. The multifrequency strategy implements the FWI method from low- to high-frequency components. A finite set of discrete frequencies is selected, and the inversion is sequentially carried out from the low- to high-frequency data components. First, the long-wavelength components of the model parameters are recovered from the low-frequency data, and then more details and features are extracted as the inversion proceeds to the higher frequency data. Fig. 1 shows the detailed workflow of the synthetic model test.

- 1) Input the actual permittivity and conductivity models and build the initial permittivity and conductivity models.
- 2) Use the finite difference time-domain (FDTD) method [21] to calculate the observed data d^{obs} and predicted data d^{pre} .
- 3) Calculate the data residual Δd . The actual measurement of the LRPR data can only be conducted in a three-dimensional (3-D) domain, which can be simplified as a point source in its far-field. An asymptotic filter is used to convert the 3-D data to its 2-D equivalent[22].
- 4) Use Wiener filtering to filter the observed data and obtain the low frequency data ($d^{obs'}$ and $d^{pre'}$). Then, calculate the backprojected data ($\Delta d' = d^{obs'} - d^{pre'}$).

- 5) Calculate and sum the gradients, which are the zero-lag correlation between the backprojected data ($\Delta d'$) and the source field.
- 6) Estimate the step-length α by the backtracking line-search method [23]. The gradients for all data are added together to update the model with TV regularization constraints.
- 7) The above steps are repeated until the normalized misfit residuals fall below a threshold and then move to the next frequency data to continue the multifrequency update strategy.

III. NUMERICAL RESULTS

The FDTD method is used to synthesize the multi-offset LRPR data [24]. According to the design of CE-5 [5],[6], the LRPR installed onboard the lander of CE-5 is approximately 90 cm above the lunar surface. Fig. 2 shows a schematic drawing of the lander of CE-5. The Vivaldi antenna elements are divided into three groups: no. 1 to no. 7 are group A, no. 8 to no. 11 are group B, and the no. 12 antennas are group C. The antenna interval within each group is 0.1 m. The distance between antenna no. 7 and no. 8 is 0.3 m [6]. The no. 12 antennas work in turn to send or receive radar signals, producing the data record in one set of measurements. The first 11 traces are signals transmitted by antenna 1 and received by the other 11 antennas. The no. 12 antenna is off-line. We only consider the in-line antenna array (1 to 11) in our 2D numerical test.

In order to ensure our numerical test resembles the actual LRPR system, we use the source wavelets obtained from the LRPR instrument ground experiments (Fig. 3). The LRPR prototype is mounted on a 1:1 model of the CE-5 lander, which includes the effect of the metallic lander and the radiation direction of the Vivaldi array antennas at the actual position [25]. Fig. 4a shows the source wavelets of all 11 transmitting antennas, which are measured in the LRPR system ground experiment. In the ground experiment, the lander is at a height of 0.89 m, and a receiving Vivaldi antenna is set under the driller (Fig. 3). There are strong noise and scattering signals in the source wavelet. Fig. 4b is the spectrum of the source wavelet. The frequency range of all antennas is from 1 GHz to 3 GHz, and the center frequency is approximately 2 GHz. In addition, the model size, antenna position, and physical parameters are also designed according to the LRPR ground experiment result of Li et al. (2018) [5].

A. Heterogeneous Lunar Layer Regolith Model Test

To evaluate the performance of the proposed FWI method in the LRPR data, we use the previous CE-3 LPR interpreted result to build the lunar layer regolith model and compute the LRPR response by the FDTD method [19]. There are 11 antennas with 0.1 m intervals in each group. The distance between antenna no. 7 and antenna no. 8 is approximately 0.3 m. The antenna array is approximately 90 cm above the surface of the Moon (Fig. 5a) [6]. According to the measurement results of the physical properties of the Apollo 16 samples [26],[27] and the interpreted result from CE-3 LPR data [19],

the permittivity of lunar regolith is from 1.5 to 5.5. To describe the heterogeneous regolith distribution, we use the Gaussian random media function [28] to generate the heterogeneous lunar regolith permittivity and conductivity distribution in Fig. 5a and 5c. Fig. 5b and 5e are the initial permittivity and conductivity models. After 40 iterations, the inverted models are shown in Figs. 5 (5c and 5f), which are close to the actual model in Fig. 5a. The lunar regolith layer interface can be accurately reconstructed in the inversion result. In addition, the local structures can also be reconstructed, and the shallow part exhibits a reliable result.

We select a 1-D depth profile for the permittivity and conductivity at distances of 0.65 m (white dashed lines in Fig. 5) slices to compare the inverted result and result of the actual model (Fig. 6). Here, the red line is the initial model, and the inverted result (black dashed line) is in agreement with the actual model (solid black line). However, there is some error in the horizontal direction. This is because the input radar wave is an approximate spherical wave diffusion. The signal amplitude in the large-angle area is too weak. For quantitative comparisons, Fig. 7 presents the data misfit curve with the proposed algorithms for the first 40 iterations. The misfit residuals of the proposed FWI decreased to 0.1 after 40 iterations. Another criterion is the data comparison that can directly measure the quality of inverted tomograms (Fig. 8). After the FWI inversion update, the last inverted traces of FWI (black dashed line) almost match the raw traces (black line). This test indicates that the LRPR FWI method provides reliable regolith physical parameter estimation and shallow lunar regolith imaging.

To evaluate the performance of the proposed FWI in noise data, we add different levels of Gaussian noise to the LRPR data. Fig. 9 are the comparison of the LRPR data with the different Gaussian noise levels (20 dB and 10 dB, respectively). Fig. 10 shows the FWI inversion result with different levels of noisy data. Both noise levels (20 dB and 10 dB) data can invert the structure of the regolith model in Fig. 5a. We also select the vertical and horizontal permittivity (black and white dashed lines in Fig. 5) slices to compare the inverted result and actual model (Fig. 11). However, the noise brings some inversion error. The interference becomes strong when the noise level increases (Fig. 11, black dashed line).

B. Lunar Regolith with Buried Rock Model Test

The primary scientific objective of the CE-5 LRPR is to probe the thickness and structure of the lunar regolith of the landing site and support the drilling and sampling process. The rocks buried in the shallow regolith are a potential threat to drilling work. A regolith model is built with a random buried rock to test the capability of the proposed FWI method in buried-rock detection. In the work of Fa et al. (2015), they divided the lunar regolith into four zones within a depth of 20 m including a reworked layered zone (1 m), an ejecta layer (2-6 m), a paleoregolith layer (4-11 m), and the underlying mare basalts [11]. The buried rock size increases with the depth, which causes substantial clutter within the ejecta. We use the same parameters as the above model test. The truly

buried rock permittivity and conductivity models are shown in Fig. 12a and 12d. The initial permittivity and conductivity models are linear gradient models, as shown in Fig. 12b and 12e. The buried rocks in the different layers are reconstructed in the FWI inversion results (Fig. 12c and 12f). In addition, the inverted permittivity parameter values are almost equal to the actual permittivity model. Fig. 13 shows the 1-D depth profiles for the permittivity and conductivity at distances of 0.65 m. Here, the red line is the initial data. The inverted result (black dashed line) is in high agreement with the actual model (black line). There is some error in the deeper part. The 2 GHz central frequency source is off-ground at 0.9 m. The signal amplitude is too weak in the deeper part. This indicates that the resolution of the more in-depth part is lower than that of the shallow area. The LRPR FWI results of the synthetic model tests can be used to evaluate the detection capability of the LRPR and help interpret the data in the CE-5 mission. The limitation is that the echoes of LRPR are more and more dissipative with the increase of the depth so that it is more difficult of deep detection at the same time the decreased resolution.

IV. CONCLUSIONS

In this paper, we utilized the multifrequency time-domain FWI with the TV constraint to evaluate the performance of CE-5 LRPR data on lunar regolith physical parameter (permittivity and conductivity) estimation and structure identification. A typical lunar regolith permittivity synthetic model is built, and the model uses the actual source wavelets of the employed Vivaldi antenna array, model size, and measurement parameters in our numerical test. The tests demonstrate that the presented FWI algorithm can provide high-resolution and reliable inversion results for the LRPR data. The effect of antenna radiation, random noise, and metal scattering can effectively be reduced or suppressed in the proposed FWI inversion, which provides a robust approach to image the regolith structure and estimates the permittivity and conductivity by the LRPR data. The synthetic model FWI inversion results demonstrate that the LRPR can meet the design requirement of a 2-m detection depth. The proposed LRPR FWI strategy provides a reliable results to determine the drilling location and avoid the risk of buried rocks. Meanwhile, there are some limitations: 1) the echoes of LRPR are more and more dissipative with the increase of the depth. The resolution become lower in the bottom regions; 2) the center frequency of the CE-5 LRPR antenna is about 2 GHz, and the maximum penetrating depth is about 3 m in the lunar regolith environment.

APPENDIX

The gradient associated with the data misfit function is derived for the 2D FWI inversion procedure.

- 1) The 2D Maxwell (1) can be written as

$$\begin{bmatrix} \epsilon \frac{\partial}{\partial t} + \sigma & -\frac{\partial}{\partial z} & \frac{\partial}{\partial x} \\ \frac{\partial}{\partial z} & \mu \frac{\partial}{\partial t} & 0 \\ \frac{\partial}{\partial x} & 0 & \mu \frac{\partial}{\partial t} \end{bmatrix} \begin{pmatrix} E_z \\ H_x \\ H_y \end{pmatrix} = \begin{pmatrix} f \\ 0 \\ 0 \end{pmatrix} \quad (13)$$

or in a more compact form

$$\mathbf{A}(\mathbf{m})\mathbf{w}(\mathbf{m}) = \mathbf{F} \quad (14)$$

where

$$\mathbf{A} = \begin{bmatrix} \epsilon \frac{\partial}{\partial t} + \sigma & -\frac{\partial}{\partial z} & \frac{\partial}{\partial x} \\ \frac{\partial}{\partial z} & \mu \frac{\partial}{\partial t} & 0 \\ \frac{\partial}{\partial x} & 0 & \mu \frac{\partial}{\partial t} \end{bmatrix}; \quad \mathbf{w} = \begin{pmatrix} E_z \\ H_x \\ H_y \end{pmatrix}$$

$$\mathbf{F} = \begin{pmatrix} f \\ 0 \\ 0 \end{pmatrix}; \quad \mathbf{m} = \begin{pmatrix} \epsilon \\ \sigma \\ \mu \end{pmatrix}. \quad (15)$$

The perturbation of the state variable \mathbf{w} with regard to the model variable \mathbf{m} is given by $\frac{\partial \mathbf{w}(\mathbf{m})}{\partial \mathbf{m}}$ and can be obtained from

$$\begin{aligned} \mathbf{A}(\mathbf{m})\mathbf{w}(\mathbf{m}) &= \mathbf{F}, \\ \Rightarrow \frac{\partial \mathbf{A}(\mathbf{m})}{\partial \mathbf{m}}\mathbf{w}(\mathbf{m}) + \mathbf{A}(\mathbf{m})\frac{\partial \mathbf{w}(\mathbf{m})}{\partial \mathbf{m}} &= \mathbf{0}, \\ \Rightarrow \frac{\partial \mathbf{w}(\mathbf{m})}{\partial \mathbf{m}} &= -\mathbf{A}^{-1}(\mathbf{m})\frac{\partial \mathbf{A}(\mathbf{m})}{\partial \mathbf{m}}\mathbf{w}(\mathbf{m}). \end{aligned} \quad (16)$$

Ignoring the amplitude normalization factor in (7), the connective function (derivative of $F_d(\mathbf{x}_r, t; \mathbf{x}_s)$) can be written as

$$\dot{F}_{\Delta d} = \langle \mathbf{A}_r \mathbf{w}_d(\mathbf{g}, \mathbf{t}; \mathbf{s}), \dot{\mathbf{w}}_{\Delta d}(\mathbf{g}, \mathbf{t}; \mathbf{s})^{\text{obs}} \rangle, \quad (17)$$

Here, \mathbf{A}_r is a restriction operator onto the receiver position and it depends on the spatial coordinates. \mathbf{w}_d denotes the predicted data for a given background permittivity and conductivity model recorded at the receiver location g due to a source excited at time $t = 0$ and at location s . $w_{\Delta d}^{\text{obs}}$ denotes the same event in the observed data.

The misfit function (5) for FWI is given by

$$\gamma = \frac{1}{2} \sum_s \sum_r \Delta d(\mathbf{g}, \mathbf{s})^2, \quad (18)$$

so that, the gradient of ϵ is

$$\begin{aligned} \frac{\partial \gamma}{\partial \epsilon} &= \sum_s \sum_g \frac{\partial \dot{F}_{\Delta d}}{\partial \epsilon(\mathbf{x})} \Delta d, \\ &= \sum_s \sum_r \frac{1}{\mathbf{K}} \frac{\partial \dot{F}_{\Delta d}}{\partial \epsilon(\mathbf{x})} \Delta d, \\ &= \sum_s \sum_r \frac{1}{\mathbf{K}} \langle \mathbf{A}_r \mathbf{w}_d(\mathbf{g}, \mathbf{t}; \mathbf{s}), \dot{\mathbf{w}}_{\Delta d}^{\text{obs}}(\mathbf{g}, \mathbf{t}; \mathbf{s}) \rangle \Delta \mathbf{d}, \\ &= \sum_s \sum_r \frac{1}{\mathbf{K}} \langle \mathbf{A}_r^{-1} \frac{\partial \mathbf{A}}{\partial \epsilon} \mathbf{w}_d(\mathbf{g}, \mathbf{t}; \mathbf{s}), \dot{\mathbf{w}}_{\Delta d}^{\text{obs}}(\mathbf{g}, \mathbf{t}; \mathbf{s}) \Delta \mathbf{d} \rangle \\ &= \sum_s \langle \frac{\partial}{\partial \epsilon} \mathbf{w}_d(\mathbf{g}, \mathbf{t}; \mathbf{s}), \frac{1}{\mathbf{A}} \sum_r (\mathbf{A}_r^* \dot{\mathbf{w}}_{\Delta d}^{\text{obs}}(\mathbf{g}, \mathbf{t}; \mathbf{s}) \Delta \mathbf{d}) \frac{1}{\mathbf{K}} \rangle \\ &= \sum_s \langle \frac{\partial}{\partial \epsilon} \mathbf{w}_d(\mathbf{g}, \mathbf{t}; \mathbf{s}), \mathbf{w}^*(\mathbf{g}, \mathbf{t}; \mathbf{s})^{\text{obs}} \rangle. \end{aligned} \quad (19)$$

According to (8), we ignore the amplitude normalization term($A(\mathbf{x}_r; \mathbf{x}_s)$)

$$\mathbf{K} = \begin{bmatrix} K_1 \\ K_2 \\ K_3 \end{bmatrix} = \begin{bmatrix} \int E_z(\mathbf{g}, \mathbf{t}; \mathbf{s}) E_z(\mathbf{g}, \mathbf{t}; \mathbf{s})^{\text{obs}} dt \\ \int H_x(\mathbf{g}, \mathbf{t}; \mathbf{s}) H_x(\mathbf{g}, \mathbf{t}; \mathbf{s})^{\text{obs}} dt \\ \int H_y(\mathbf{g}, \mathbf{t}; \mathbf{s}) H_y(\mathbf{g}, \mathbf{t}; \mathbf{s})^{\text{obs}} dt \end{bmatrix}, \quad (20)$$

$\mathbf{w}^* = [\hat{E}_z, \hat{H}_x, \hat{H}_y]^T$ is the adjoint-state variable of $\mathbf{w} = [E_z, H_x, H_y]^T$ and is calculated by finite-difference solution of the adjoint-state equations.

$$\begin{bmatrix} \epsilon \frac{\partial}{\partial t} + \sigma & -\frac{\partial}{\partial z} & \frac{\partial}{\partial x} \\ \frac{\partial}{\partial z} & \mu \frac{\partial}{\partial t} & 0 \\ \frac{\partial}{\partial x} & 0 & \mu \frac{\partial}{\partial t} \end{bmatrix} \begin{pmatrix} \hat{E}_z \\ \hat{H}_x \\ \hat{H}_y \end{pmatrix} = \begin{pmatrix} \hat{f} \\ 0 \\ 0 \end{pmatrix} \quad (21)$$

Here,

$$\hat{f} = \sum_g \mathbf{A}_r^* \Delta \mathbf{D}(\mathbf{g}, \mathbf{t}; \mathbf{s}), \quad (22)$$

where $\Delta D(\mathbf{g}, \mathbf{t}; \mathbf{s})$ denotes the data residual of all LPR data. With (15), we can derive:

$$\frac{\partial \mathbf{A}}{\partial \epsilon} = \begin{bmatrix} \frac{\partial}{\partial t} & 0 & 0 \\ 0 & 0 & 0 \\ 0 & 0 & 0 \end{bmatrix}, \quad (23)$$

$$\frac{\partial \mathbf{A}}{\partial \sigma} = \begin{bmatrix} 1 & 0 & 0 \\ 0 & 0 & 0 \\ 0 & 0 & 0 \end{bmatrix}, \quad (24)$$

Using (19) and (23), we can get the gradient of permittivity (ϵ),

$$\begin{aligned} \frac{\partial \gamma}{\partial \epsilon} &= \sum_s \langle \frac{\partial \mathbf{A}}{\partial \epsilon} \mathbf{w}_d(\mathbf{g}, \mathbf{t}; \mathbf{s}), \mathbf{w}^*(\mathbf{g}, \mathbf{t}; \mathbf{s})^{\text{obs}} \rangle, \\ &= \sum_s \langle \begin{bmatrix} \frac{\partial}{\partial t} & 0 & 0 \\ 0 & 0 & 0 \\ 0 & 0 & 0 \end{bmatrix} \begin{bmatrix} E_z \\ H_x \\ H_y \end{bmatrix}, \begin{bmatrix} \hat{E}_z \\ \hat{H}_x \\ \hat{H}_y \end{bmatrix} \rangle, \\ &= \sum_s \int (\frac{\partial E_z}{\partial t} \hat{E}_x) dt. \end{aligned} \quad (25)$$

The dot product of the backpropagated residual vector and the source-field vector integrated over time is the correlation imaging condition [29].

REFERENCES

- [1] L. Xiao *et al.*, "A young multilayered terrane of the northern Mare Imbrium revealed by Chang'E-3 mission," *Science*, vol. 347, no. 6227, pp. 1226-1229, Mar. 2015.
- [2] G. Y. Fang, B. Zhou, and Y. C. Ji, "Lunar penetrating radar onboard the Chang'E-3 mission," *Research in Astronomy and Astrophysics*, vol. 14, no. 12, pp. 1607-1622, Dec. 2014.
- [3] Y. Su, G. Y. Fang, and J. Q. Feng, "Data processing and initial results of Chang'E-3 lunar penetrating radar," *Research in Astronomy and Astrophysics*, vol. 14, no. 12, pp. 1623-1632, Dec. 2014.
- [4] Y. Z. Jia *et al.*, "Scientific objectives and payloads of Chang'E-4 mission," *Chin. J. Space Sci.*, vol. 38, no. 1, pp. 118-130, Jan. 2018.
- [5] Y. Li, W. Lu, G. Fang, B. Zhou, and S. Shen, "Performance verification of lunar regolith penetrating array radar of Chang'E-5 mission," *Advances in Space Research*, vol. 63, no. 7, pp.2267-2278, Jul. 2019.
- [6] Y. Li, W. Lu, G. Fang, and S. Shen, "The imaging method and verification experiment of Chang'E-5 lunar regolith

- penetrating array radar,” *IEEE Geoscience and Remote Sensing Letters*, vol. 15, no. 7, pp. 1006-1011, Jul. 2018.
- [7] E. Forte, and M. Pipan, “Review of multi-offset GPR applications: data acquisition, processing and analysis,” *Signal Processing*, vol. 132, pp. 210-220, Mar. 2017.
- [8] P. Williamson, and M. Worthington, “Resolution limits in ray tomography due to wave behavior: numerical experiments,” *Geophysics*, vol. 58, pp. 727-735, May 1993.
- [9] P. Mora, “Nonlinear two-dimensional elastic inversion of multi-offset seismic data,” *Geophysics*, vol. 52, no. 9, pp. 1211-1228, Sep. 1987.
- [10] J. Virieux, and S. Operto, “An overview of full-waveform inversion in exploration geophysics,” *Geophysics*, vol. 74, no. 6, pp. 1-26, June 2009.
- [11] D. Feng, C. Cao and X. Wang, “Multiscale full-waveform dual-parameter inversion based on total variation regularization to on-ground GPR data,” *IEEE Transactions on Geoscience and Remote Sensing*, vol. 57, no. 11, pp. 9450-9465, Nov. 2019.
- [12] D. Feng, X. Wang and X. Wang, “New dynamic stochastic source encoding combined with a minmax-concave total variation regularization strategy for full waveform inversion,” *IEEE Transactions on Geoscience and Remote Sensing*, vol. 58, no. 11, pp. 7753-7771, Nov. 2020.
- [13] N. Huai, Z.F. Zeng, J. Li, Y. Yan and Q. Lu, “Model-based layer stripping FWI with a stepped inversion sequence for GPR data,” *Geophysical Journal International*, vol. 218, no. 2, pp.1032-1043, Aug. 2019.
- [14] L. Sirgue and R. G. Pratt, “Efficient waveform inversion and imaging: A strategy for selecting temporal frequencies,” *Geophysics*, vol. 69, no. 1, pp. 231-248, Jan. 2004.
- [15] W. Pan, Y. Geng and K. Innanen, “Interparameter trade-off quantification and reduction in isotropic-elastic full-waveform inversion: synthetic experiments and Hussar land data set application,” *Geophysical Journal International*, vol. 213, no. 2, pp.1305-1333, Aug. 2018.
- [16] H. Aghamiry, A. Gholami and S. Operto, “Hybrid Tikhonov + total-variation regularization for imaging large-contrast media by full waveform inversion,” *SEG International Exposition and 88th annual Meeting*, 2018, pp.1253-1258.
- [17] Apollo Preliminary Examination Team, “The Apollo 15 Lunar Samples: a preliminary description,” *Science*, vol. 175, no. 4020, pp. 363-375, Jan. 1972.
- [18] W. Fa, M. Zhu, T. Liu, and J. B. Plescia, “Regolith stratigraphy at the Chang’E-3 landing site as seen by lunar penetrating radar,” *Geophys. Res. Lett.*, vol. 42, pp. 10179-10187, Dec. 2015.
- [19] J. Li, Z. Zeng, C. Liu, N. Huai, and K. Wang, “A Study on Lunar Regolith Quantitative Random Model and Lunar Penetrating Radar Parameter Inversion,” *IEEE Geoscience and Remote Sensing Letters*, vol. 14, no. 11, pp. 1953-1959, Nov. 2017.
- [20] Y. Luo, G. T. Schuster, “Wave-equation travelttime inversion,” *Geophysics*, vol. 56, pp. 645-653, 1991.
- [21] H. Liu, X. Y. Huang, F. Han, J. Cui, B. F. Spencer, and X. Y. Xie, Hybrid Polarimetric GPR Calibration and Elongated Object Orientation Estimation,” *IEEE Journal of Selected Topics in Applied Earth Observations and Remote Sensing*, vol. 12, no. 7, pp. 2080-2087, July 2019.
- [22] H. Liu, Z. Long, B. Tian, F. Han, G. Fang, and H. Liu, “Two-Dimensional Reverse-Time Migration Applied to GPR With a 3-D-to-2-D Data Conversion,” *IEEE Journal of Selected Topics in Applied Earth Observations and Remote Sensing*, vol. 10, no. 10, pp. 4313-4321, Oct. 2017.
- [23] J. Nocedal, and S. Wright, “*Numerical optimization*,” Springer Series in Operations Research, Springer Company, vol. 35, 1999.
- [24] J. Li, Z. Zeng, L. Huang, and F. Liu, “GPR simulation based on complex frequency shifted recursive integration PML boundary of 3D high order FDTD,” *Computers Geosciences*, vol. 49, pp. 121-130, Dec. 2012.
- [25] Y. Xiao, Y. Su, S. Dai, J. Feng, S. Xing, C. Ding and C. Li, “Ground experiments of Chang’E-5 lunar regolith penetrating radar,” *Advances in Space Research*, vol. 63, pp. 3404-3419, Jan. 2019.
- [26] G. H. Heiken, D. T. Vaniman, and B. M. French, “*Physical properties of the lunar surface, in Lunar Sourcebook: A User Guide to the Moon*,” Cambridge, U.K. Cambridge Univ. Press, pp. 530-558, 1991.
- [27] G. Olhoeft, A. Frisillo and D. Strangway, “Temperature dependence of electrical conductivity and lunar temperatures,” *Moon*, vol. 9, pp. 79-87, Mar. 1974.
- [28] Z. Jiang, Z. Zeng, J. Li, F. Liu, and W. Li, “Simulation and analysis of GPR signal based on stochastic media model with an ellipsoidal autocorrelation function,” *J. Appl. Geophys.*, vol. 99, no. 1, pp. 91-97, Jan. 2013.
- [29] J. Li, G. Dutta, G. Schuster, “Wave-equation Qs inversion of skeletonized surface waves,” *Geophysical Journal International*, vol. 209, pp. 979-991, May. 2017.

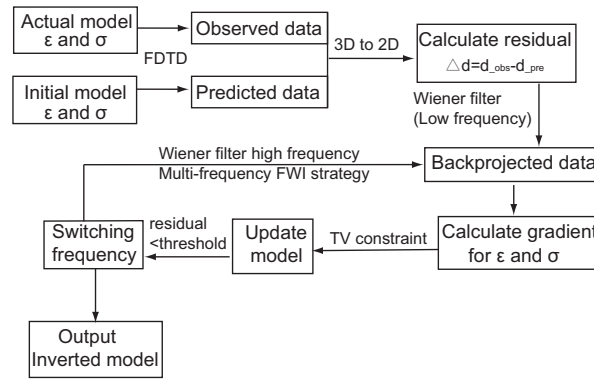


Fig. 1. Flow chart of the LRPR multi-frequency FWI with TV constraint algorithms.

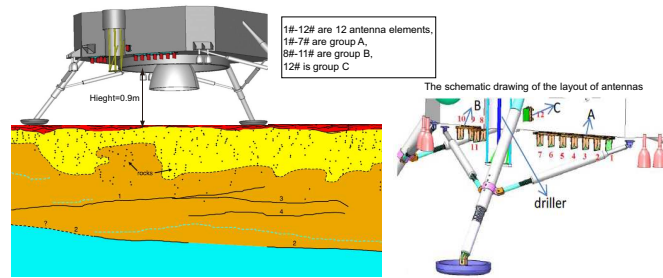


Fig. 2. Schematic of the LRPR system. 12 Vivaldi antenna elements are divided into three groups. 1-7 are group A, 8-11 are group B, and 12 is group C. The antenna array is about 90 cm height from the lunar surface [6].



Fig. 3. Photographs of the test site and the setup of the LRPR ground experiments, modify from [6].

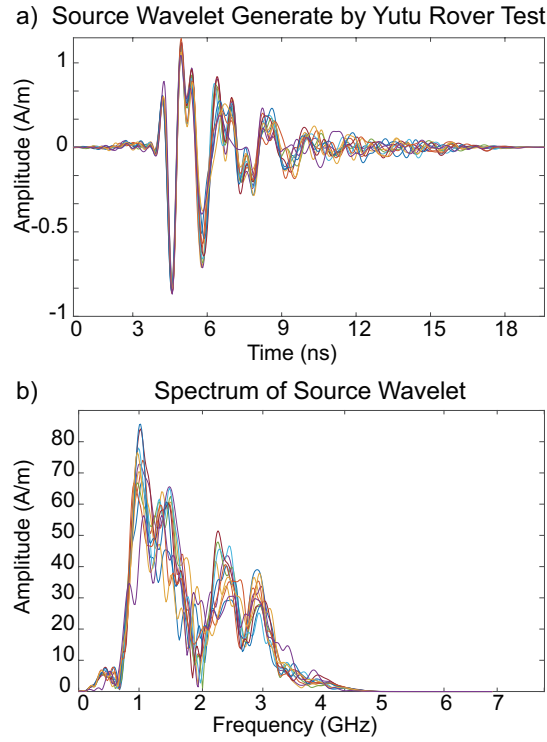


Fig. 4. (a) The source wavelet which is measured by ground LPR experiment test (The difference color lines are the actual source of 12 Vivaldi antenna elements). b) The spectrum of the source wavelet.

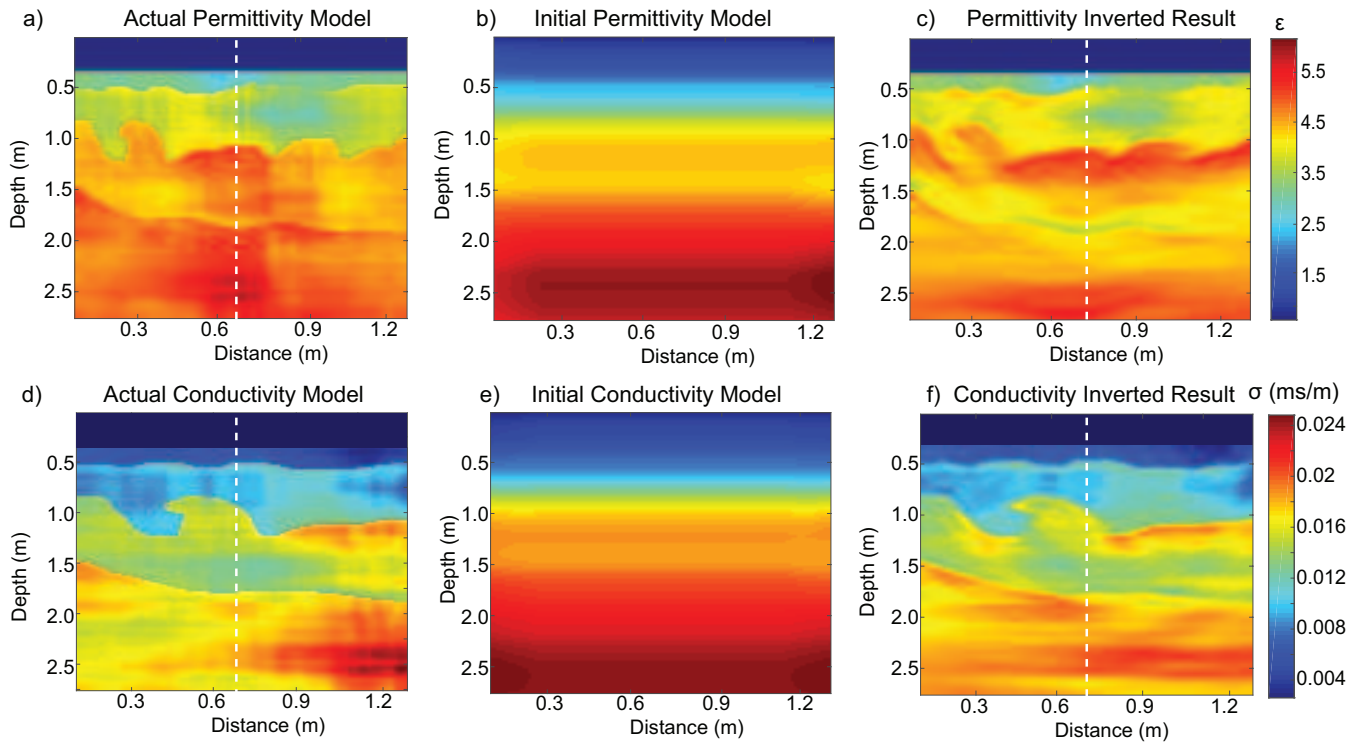


Fig. 5. a) and d) are lunar regolith with buried rock model; b) and e) are initial model; c) and f) are FWI inversion result.

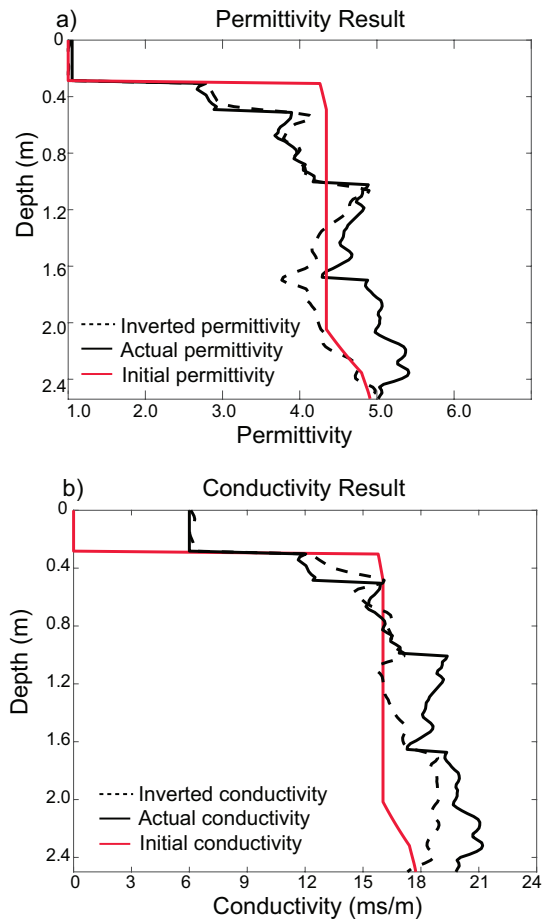


Fig. 6. a) and b) are 1-D depth profiles for the permittivity and conductivity at distances of 0.65 m (dashed white lines in Fig. 5a and 5c).

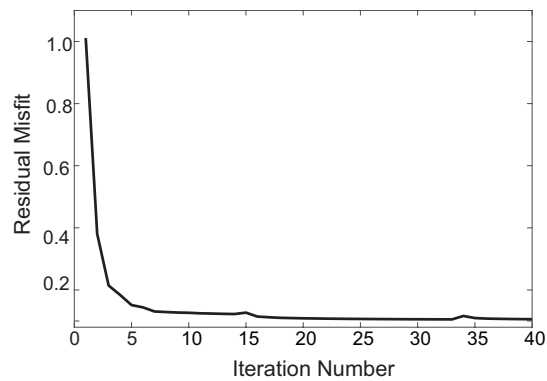


Fig. 7. The residual misfit vs iteration times.

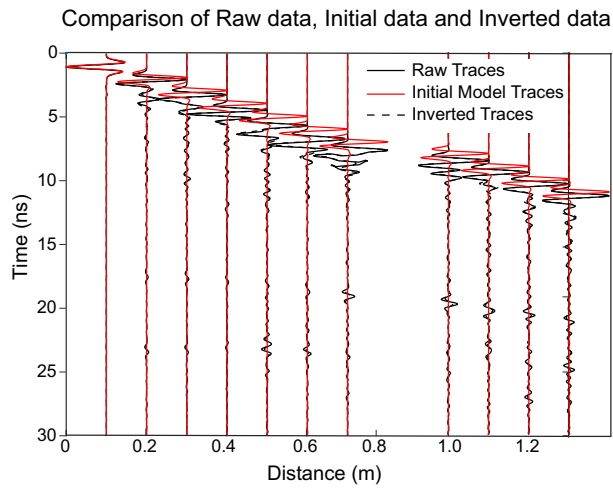


Fig. 8. LRPR data generated by the source placed at the first antenna location. The black and red traces are observed data and the data of the initial model, and the dashed black line is the inverted data.

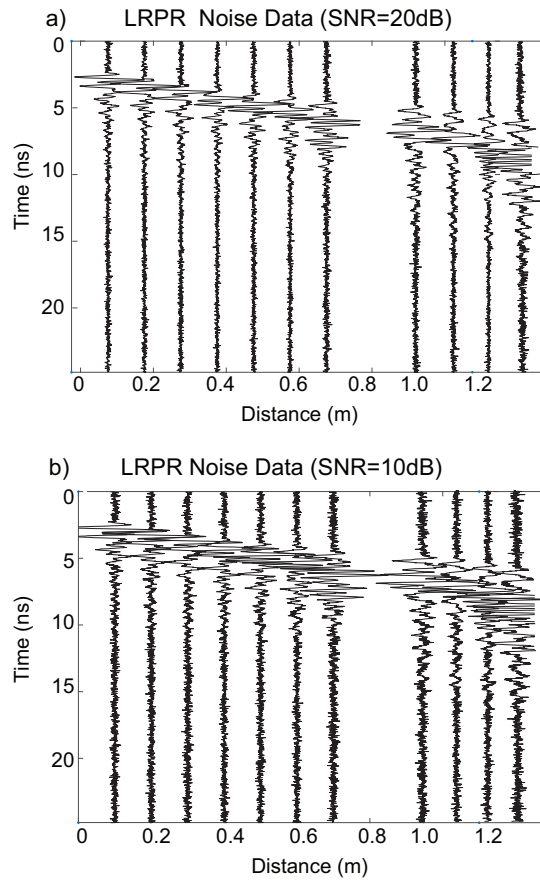


Fig. 9. LRPR data generated by the source placed at the first source location data with different Gaussian noise level, SNR=20dB and 10dB, respectively.

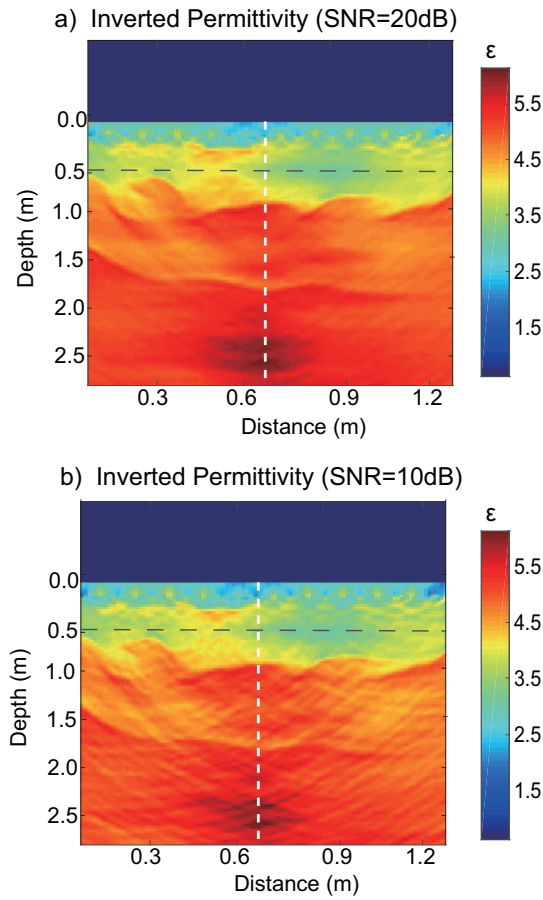


Fig. 10. a) FWI lunar regolith permittivity inversion result with Gaussian noise (SNR=20dB); b) FWI lunar regolith permittivity inversion result with Gaussian noise (SNR=10dB).

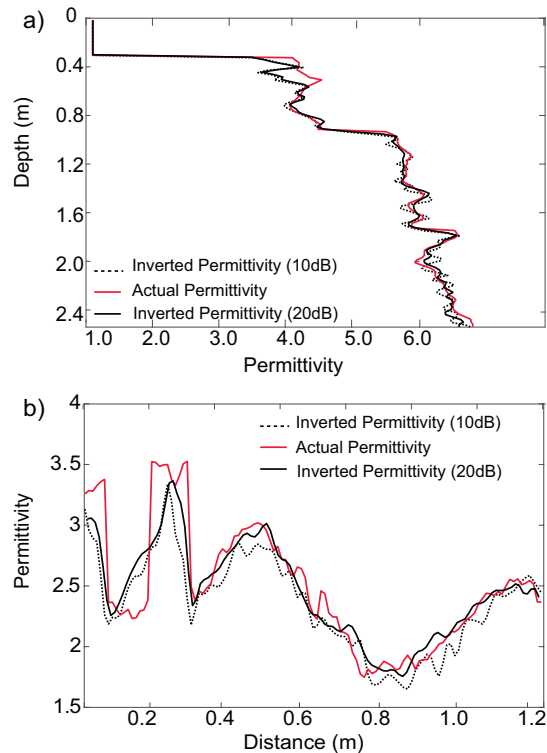


Fig. 11. a) 1-D depth profiles for the permittivity at distances of 0.65 m; b) Parameter section of permittivity at $z = 0.5$ m (dashed white and black lines in Fig. 10a(SNR=20dB) and Fig. 10b(SNR=10dB)).

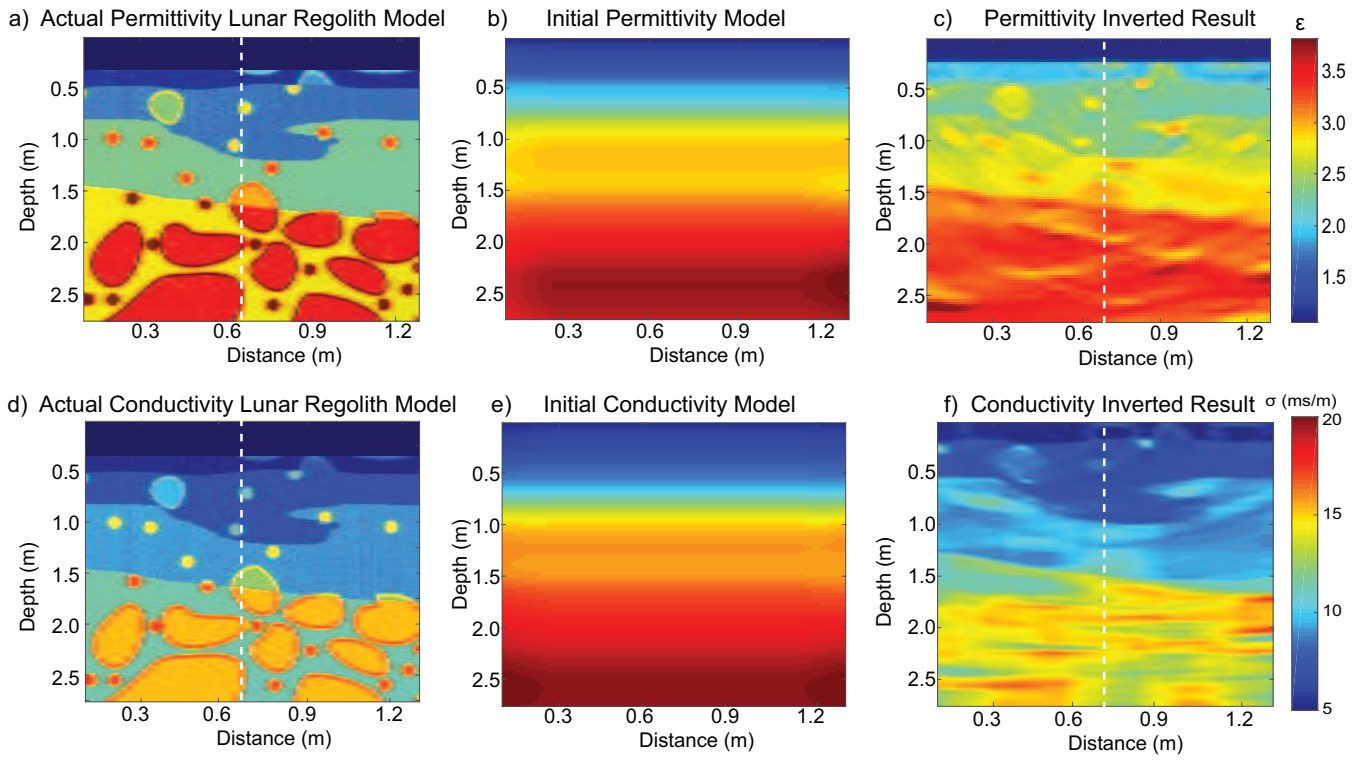


Fig. 12. a) and d) are lunar regolith with buried rock model; b) and e) are initial model; c) and f) are FWI inversion result.

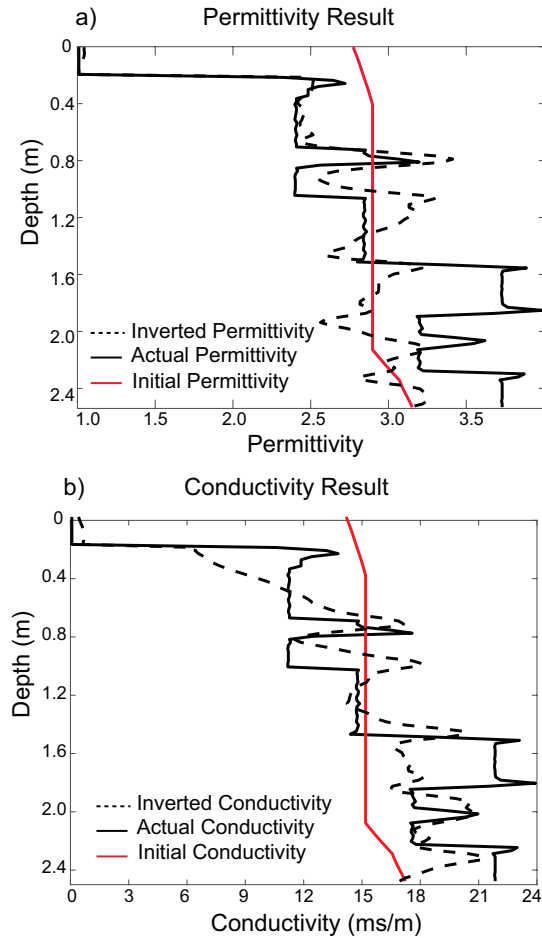


Fig. 13. a) and b) are 1-D depth profiles for the permittivity and conductivity at distances of 0.65 m (dashed white lines in Fig. 12a and 12c).